


MATERIALS SCIENCE

Tuning 2D magnetism in $\text{Fe}_{3+X}\text{GeTe}_2$ films by element doping

Shanshan Liu^{1,2,†}, Zihan Li^{1,2,†}, Ke Yang^{3,4,†}, Enze Zhang^{1,2}, Awadhesh Narayan⁵, Xiaoqian Zhang⁶, Jiayi Zhu⁷, Wenqing Liu⁸, Zhiming Liao^{9,10}, Masaki Kudo¹¹, Takaaki Toriyama¹¹, Yunkun Yang^{1,2}, Qiang Li^{1,2}, Linfeng Ai^{1,2}, Ce Huang^{1,2}, Jiabao Sun⁸, Xiaojiao Guo¹², Wenzhong Bao¹², Qingsong Deng¹⁰, Yanhui Chen¹⁰, Lifeng Yin^{1,2,13}, Jian Shen^{1,2,13}, Xiaodong Han¹⁰, Syo Matsumura^{11,14}, Jin Zou^{9,15}, Yongbing Xu⁶, Xiaodong Xu⁷, Hua Wu^{1,4,13,*} and Faxian Xiu ^{1,2,13,16,*}

¹State Key Laboratory of Surface Physics and Department of Physics, Fudan University, Shanghai 200433, China; ²Institute for Nanoelectronic Devices and Quantum Computing, Fudan University, Shanghai 200433, China; ³College of Science, University of Shanghai for Science and Technology, Shanghai 200093, China; ⁴Laboratory for Computational Physical Sciences (MOE), Fudan University, Shanghai 200433, China; ⁵Solid State and Structural Chemistry Unit, Indian Institute of Science, Bangalore 560012, India;

(Continued on next page)

*Corresponding authors. E-mails: Faxian@fudan.edu.cn; wuh@fudan.edu.cn

[†]Equally contributed to this work.

Received 20 August 2020; Revised 24 February 2021; Accepted 10 June 2021

ABSTRACT

Two-dimensional (2D) ferromagnetic materials have been discovered with tunable magnetism and orbital-driven nodal-line features. Controlling the 2D magnetism in exfoliated nanoflakes via electric/magnetic fields enables a boosted Curie temperature (T_C) or phase transitions. One of the challenges, however, is the realization of high T_C 2D magnets that are tunable, robust and suitable for large scale fabrication. Here, we report molecular-beam epitaxy growth of wafer-scale $\text{Fe}_{3+X}\text{GeTe}_2$ films with T_C above room temperature. By controlling the Fe composition in $\text{Fe}_{3+X}\text{GeTe}_2$, a continuously modulated T_C in a broad range of 185–320 K has been achieved. This widely tunable T_C is attributed to the doped interlayer Fe that provides a 40% enhancement around the optimal composition $X = 2$. We further fabricated magnetic tunneling junction device arrays that exhibit clear tunneling signals. Our results show an effective and reliable approach, i.e. element doping, to producing robust and tunable ferromagnetism beyond room temperature in a large-scale 2D $\text{Fe}_{3+X}\text{GeTe}_2$ fashion.

Keywords: 2D ferromagnetic material, $\text{Fe}_{3+X}\text{GeTe}_2$ film, element doping, above room temperature, T_C tunability

INTRODUCTION

Since the discovery of van der Waals two-dimensional (2D) materials, especially graphene [1], such 2D crystals have been widely extended to transition metal dichalcogenides [2] and 2D superconductors [3]. More recently, 2D magnets have attracted enormous attention because of the emergence of ferromagnetism in the monolayer limit [4,5]. Novel theoretical proposals and experiments in magnetic tunability and spintronic devices have been reported. Theoretically, moiré skyrmions [6], the nodal-line property [7], the quantum anomalous Hall effect [8] and the ‘magic angle’ effect on magnetism [9,10] have been proposed in 2D magnets and their heterostructures. Magneto-band-structure effect [11], described as

the electronic band structure modified by magnetization directions, has also been predicted in 2D van der Waals ferromagnetic materials for the realization of giant magnetoresistance. Experimentally, the rapid exploration of new 2D ferromagnets provides a fertile ground for exotic magnetic properties, for instance, Curie temperature (T_C) and coercive field (H_C) tunability via gate voltage [12,13], magnon-assisted tunneling [14] and giant magnetoresistance [15–17]. In spite of the tremendous progress made in the CrX_3 system, its T_C remains below 60 K and the exploration of high T_C materials becomes particularly appealing. Fe_3GeTe_2 exhibits a relatively high T_C of ~ 220 K in the bulk state with a strong perpendicular magnetic anisotropy [18]. In exfoliated Fe_3GeTe_2 nanoflakes with a sample

size in the order of micrometers, T_C achieves a high modulation even up to room temperature via ionic liquid gating [19]. Characterized by magnetotransport and angle-resolved-photoemission spectroscopy, the bulk Fe_3GeTe_2 is proposed to be a ferromagnetic nodal-line semimetal [7] that promises more exotic properties like magnetically tunable nodes [20,21]. An intriguing proposal, with regard to such materials, is to realize the quantized anomalous Hall effect at significantly higher temperatures in the monolayer limit [22,23]. However, the approach to achieving controllable growth with large-scale functioning devices and high- T_C ferromagnetic order remains elusive to date.

Chemical doping, via intentionally introducing impurities into parent materials, has been established as a direct yet effective approach to modulating and functionalizing the intrinsic electronic properties of 2D materials [24,25]. Doped transition metal dichalcogenides exhibit tunable electronic and optoelectronic properties [26–29]. Through Cr doping, the quantized anomalous Hall effect at millikelvin temperatures was discovered in Cr-doped $(\text{Bi, Sb})_2\text{Te}_3$ films [30]. Dilute magnetic semiconductors, such as $(\text{Ga, Mn})\text{As}$, yield a large modulation of T_C with different Mn compositions [31,32]. Scenarios of nitrogen-decorated NbSe_2 nanosheets show the coexistence of ferromagnetism and superconductivity [33]. In $\text{Fe}_{3-X}\text{GeTe}_2$ bulk crystals [34] and films made by molecular-beam epitaxy (MBE) [35], the ferromagnetic behavior of T_C undergoes a monotonically decreasing trend with the reduction of the Fe composition. Nevertheless, the atom-doping-engineered T_C in 2D materials remains lower than 250 K, and further effective methods for magnetism modulation and the investigation into the underlying mechanism are indispensable.

Here, we employ a precise control of element flux in MBE to directly accomplish a T_C of 320 K in wafer-scale $\text{Fe}_{3+1.80}\text{GeTe}_2$ films. Aberration-corrected scanning transmission electron microscopy (STEM) investigations confirm the well-preserved layered structure in Fe-rich films. The angle-dependent anomalous Hall effect (AHE) evidences the persistent perpendicular magnetic anisotropy up to its T_C of 320 K, which is consistent with that deduced from zero-field-cooled (ZFC) and field-cooled (FC) susceptibility results ($T_C \sim 316.1$ K) and X-ray magnetic circular dichroism results (XMCD, $T_C \sim 313.3$ K). The T_C of the $\text{Fe}_{3+X}\text{GeTe}_2$ films is found to be strongly dependent on the X value, which continuously increases from ~ 185 K ($X = -0.25$) to 320 K

($X = 1.80$) followed by the decreasing behavior to 290 K at $X = 2.80$. Density functional theory (DFT) calculations confirm the ferromagnetic ground state of the bulk Fe_3GeTe_2 via a comparison with different antiferromagnetic states. Moreover, the calculations find that the doped interlayer Fe atoms contribute significantly to the T_C enhancement. Based on these high-quality thin films, $\text{Fe}_{3+0.76}\text{GeTe}_2/\text{MgO}/\text{Fe}_3\text{GeTe}_2$ magnetic tunneling junction (MTJ) arrays are fabricated and clear tunneling signals are distinguished with a low-temperature tunneling magnetoresistance (TMR) ratio of $\sim 0.25\%$.

$\text{Fe}_{3+X}\text{GeTe}_2$ FILM SYNTHESIS

The layered Fe_3GeTe_2 compound has a hexagonal structure with the lattice parameters of $a = 3.991(1)$ Å, $c = 16.33(3)$ Å and a space group of $P6_3/mmc$ [36]. Figure 1a shows the projection view of the Fe_3GeTe_2 atomic structure along the $[01-10]$ zone-axis, in which each layer consists of five sub-layers [36] with a Fe_3Ge slab sandwiched between two neighboring Te layers with the corresponding nominal valence state of $(\text{Te}^{2-})(\text{Fe}^{3+})[(\text{Fe}^{2+})(\text{Ge}^{4+})](\text{Fe}^{3+})(\text{Te}^{2-})$. By controlling the growth temperature and the flux of each element, high-crystalline $\text{Fe}_{3+X}\text{GeTe}_2$ films can be successfully grown by MBE. Figure 1b is an X-ray diffraction (XRD) pattern taken from a representative film, from which diffraction peaks can be ascribed to a series of $\{0002\}$ planes (PDF# 75–5620). Its inset displays a streaky *in-situ* reflection high-energy electron diffraction (RHEED) pattern, indicative of a layer-by-layer growth mode for Fe-doped $\text{Fe}_{3+X}\text{GeTe}_2$ films (also displayed in Fig. S1). Figure 1c is a STEM-high angle annular dark-field (HAADF) image taken from a typical cross section of the film and shows the layered structure with an interlayer distance of ~ 0.8 nm (close to the determined value for the stoichiometric Fe_3GeTe_2 films [35,37]). Therefore, the layered structure and high crystalline quality in Fe-rich $\text{Fe}_{3+X}\text{GeTe}_2$ thin films are well preserved. Figure 1d shows the corresponding X-ray energy dispersive spectrometry (EDS) profile of the film, and the quantitative analysis suggests the composition of the epitaxial $\text{Fe}_{3+X}\text{GeTe}_2$ is $\text{Fe}_{3+1.06}\text{GeTe}_2$. The left inset is a photograph of a 2-inch $\text{Fe}_{3+1.06}\text{GeTe}_2$ film, and the right inset shows an average surface roughness of 0.32 nm in the area of $10 \mu\text{m} \times 10 \mu\text{m}$ detected by atomic force microscopy.

(Continued from previous page)

⁶School of Electronic Science and Engineering, Nanjing University, Nanjing 210093, China;

⁷Department of Physics, University of Washington, Seattle, WA 98195-1560, USA;

⁸Department of Electronic Engineering, Royal Holloway University of London, Egham TW20 0EX, UK;

⁹Materials Engineering, The University of Queensland, Brisbane QLD 4072, Australia;

¹⁰Beijing Key Laboratory of Microstructure and Property of Advanced Materials, Institute of Microstructure and Property of Advanced Materials, Beijing University of Technology, Beijing 100124, China;

¹¹The Ultramicroscopy Research Center, Kyushu University, Fukuoka 819-0395, Japan;

¹²State Key Laboratory of ASIC and System, School of Microelectronics, Fudan University, Shanghai 200433, China;

¹³Collaborative Innovation Center of Advanced Microstructures, Nanjing 210093, China;

¹⁴Department of Applied Quantum Physics and Nuclear Engineering, Kyushu University, Fukuoka 819-0395, Japan;

¹⁵Centre for Microscopy and Microanalysis, The University of Queensland, Brisbane QLD 4072, Australia and

¹⁶Shanghai Research Center for Quantum Sciences, Shanghai 201315, China

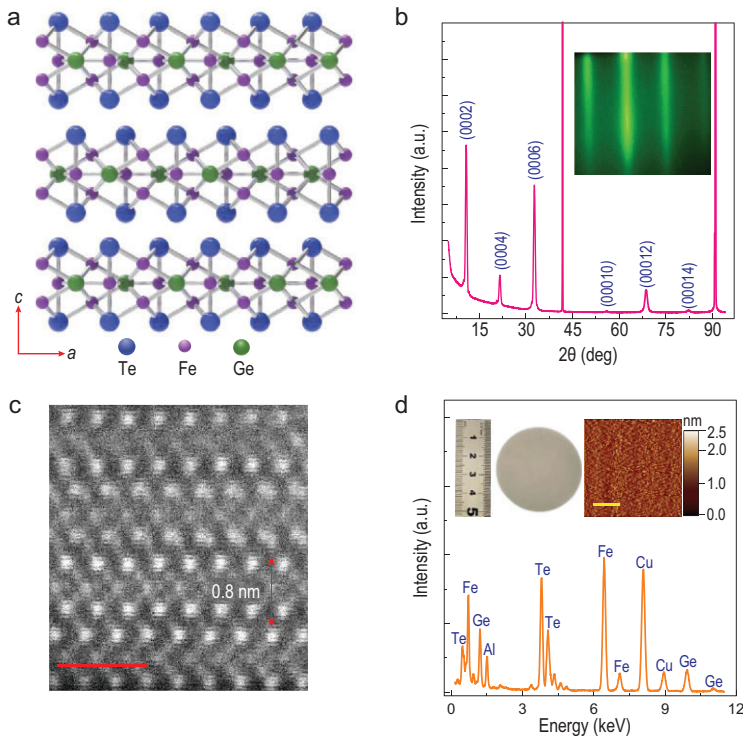


Figure 1. 2D layered structure in $\text{Fe}_{3+\chi}\text{GeTe}_2$ thin films. (a) Fe_3GeTe_2 structure geometry. (b) XRD spectrum from $\text{Fe}_{3+0.18}\text{GeTe}_2$, with the peaks ascribed to (0002), (0004), (0006), (00010), (00012) and (00014) according to PDF# 75-5620. Inset, an RHEED pattern. (c) A cross section HAADF image of $\text{Fe}_{3+1.06}\text{GeTe}_2$. Layered structure with an interlayer distance of 0.8 nm is well-preserved in such Fe-rich films. The scale bar is 1 nm. (d) EDS for $\text{Fe}_{3+1.06}\text{GeTe}_2$. Left inset, a photograph of a 2-inch $\text{Fe}_{3+1.06}\text{GeTe}_2$ film. Right inset, an atomic force microscopy image taken from a $10\ \mu\text{m} \times 10\ \mu\text{m}$ surface, showing the average surface roughness of 0.32 nm. The scale bar is $3\ \mu\text{m}$.

ROOM-TEMPERATURE FERROMAGNETISM IN $\text{Fe}_{3+1.80}\text{GeTe}_2$ FILM

To experimentally probe the high- T_C ferromagnetism in $\text{Fe}_{3+1.80}\text{GeTe}_2$ films, we carried out magnetotransport and M - H measurements. Unless specifically mentioned, hereafter, the thickness of Fe_3GeTe_2 films is ~ 10 nm. The Hall effect for general ferromagnetic materials can be described as

$$R_{xy} = R_H B + R_{AH} M,$$

where the Hall coefficient R_H stands for the ordinary Hall effect that is linearly dependent on the magnetic field (B), and the anomalous Hall effect $R_{AH}M$ comes from the magnetization (M) contribution. The AHE component can be obtained by subtracting the linear Hall resistance from the total Hall effect data, as illustrated in Fig. 2a. By increasing the temperature, the coercive field (H_C) decreases correspondingly. Up to 300 K, the anomalous Hall resistance (R_{XY}) still shows a hysteresis as the magnetic field scans back and forth; and eventually H_C vanishes at 330 K (Fig. 2a inset), based

on which T_C is estimated to be ~ 320 K. It should be noted that in exfoliated Fe_3GeTe_2 , perpendicular magneto-crystalline anisotropy persists to monolayer even though T_C has been largely suppressed [19].

To characterize the Fe-doping effect on its magnetic anisotropy, the angle-dependent AHE at different temperatures is investigated. Here, the angle θ is defined as the angle between the magnetic field and the normal vector of the sample surface, as illustrated in the inset of Fig. 2b. At 2.5 K, the easy axis is confirmed to be along the out-of-plane direction with a perpendicular magnetic anisotropy due to the fact that the H_C increases simultaneously with the angle rotating from 0° to 90° , thus sharing the same anisotropy property as the stoichiometric Fe_3GeTe_2 [35]. This perpendicular anisotropy persists up to 320 K, as verified by the angle-dependent AHE at 270 K, 300 K and 320 K, shown in Fig. S7. Analyzed with the Stoner-Wohlfarth model [19,38], the perpendicular magneto-crystalline anisotropy energy density (K_u) is estimated to be $\sim 1.08 \times 10^7$ erg/cm $^{-3}$ (Supplementary Note S2), which is comparable to that of the Fe_3GeTe_2 bulk crystals [38]. We have further explored the zero-field-cooled/field-cooled (ZFC-FC) magnetization curves for $\text{Fe}_{3+1.80}\text{GeTe}_2$ film (Fig. 2c, details in Supplementary Note S3), which exhibit different trends as the temperature decreases; they start to separate at ~ 320 K. The variation of magnetization as a function of temperature is positively proportional to the magnetic susceptibility, which can be fitted by the Curie-Weiss law

$$\chi = \chi_0 + C/(T - T_C),$$

where χ_0 is a temperature-independent parameter resulting from the density of states at the Fermi energy level, and C is the Curie constant. The best fit to the experimental FC curve yields a T_C of 316.1 ± 2.6 K (Fig. 2c inset), consistent with the value tracked from the temperature-dependent AHE (Fig. 2a). The M - H curves at different temperatures are illustrated in Fig. S12a, where the coercive field of 40 Oe can be distinguished at 300 K.

Now the global room-temperature ferromagnetism in the millimeter-level flakes has been verified both by AHE and magnetization measurement. We further carried out the surface-sensitive polar reflective magnetic circular dichroism (RMCD) measurement where the focused laser spot was $\sim 3\ \mu\text{m}$ to investigate its local magnetism. Figure 2d displays temperature-dependent RMCD measurement as a function of B . Consistent with the decreasing H_C and R_{XY} in the AHE measurements, the H_C and remanent magnetization decrease with the increasing temperature.

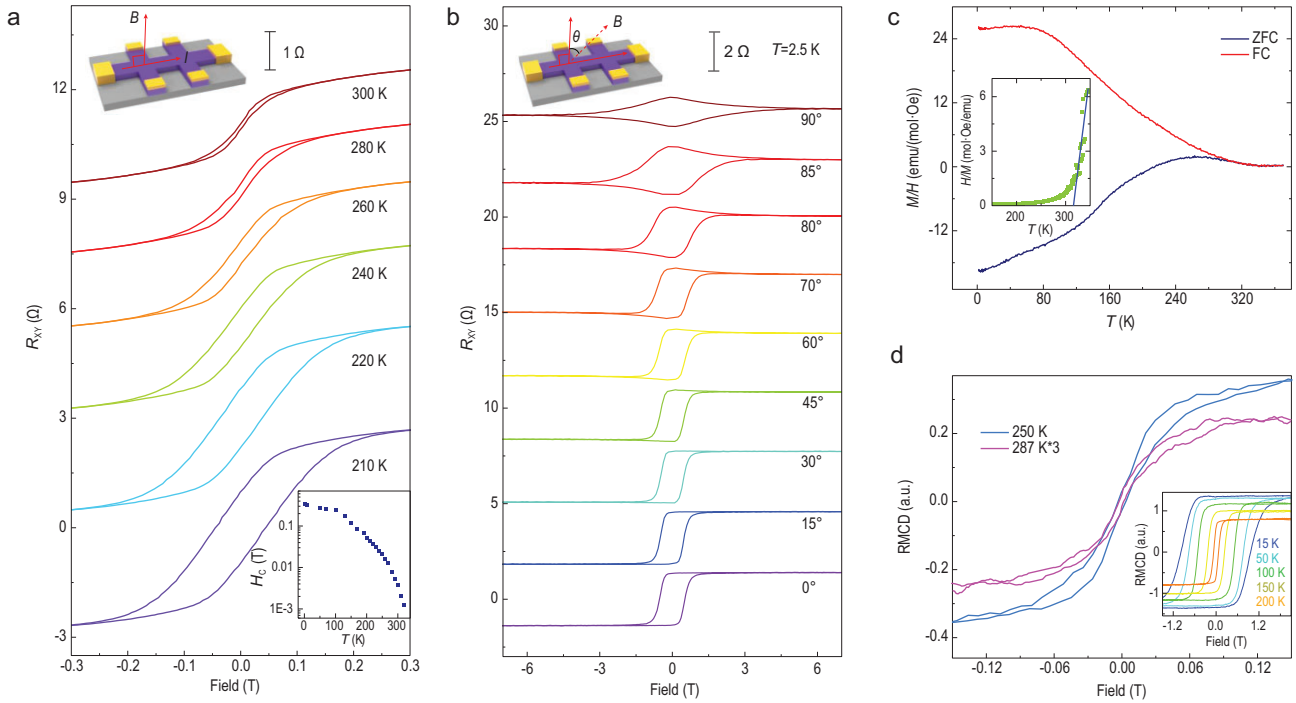


Figure 2. Out-of-plane ferromagnetic anisotropy of $\text{Fe}_{3+1.80}\text{GeTe}_2$ film with T_C of ~ 320 K. (a) Temperature-dependent AHE under the perpendicular measurement geometry. Top inset, a schematic configuration of the perpendicular geometry between the sample surface and the magnetic field. Bottom inset, coercive field tracked from AHE. Up to 320 K, visible hysteresis can be distinguished, and vanishes at 330 K. T_C can be determined to be ~ 320 K. (b) Angle-dependent AHE at 2.5 K. Because H_C increases with θ tilting from 0° to 90° , the easy axis is determined to be out-of-plane. Inset, the schematic geometry that defines the angle θ . (c) Zero-field-cooled (ZFC) and field-cooled (FC) susceptibility curves under a magnetic field of 200 Oe. T_C is determined to be 316.1 ± 2.6 K by the Curie-Weiss law as shown in the inset. The detailed estimation process is described in Supplementary Note S3. (d) Temperature-dependent polar RMCD curves. H_C and remanent magnetization decrease as the temperature increases, while ferromagnetic order still exists at 287 K.

It remains visible at 287 K and therefore confirms the enhanced ferromagnetism and the film uniformity. Combined with the persistent perpendicular magneto-crystalline anisotropy at various temperatures (Figs 2b and S7), this high T_C behavior in $\text{Fe}_{3+1.80}\text{GeTe}_2$ films can be confirmed and the presence of either Fe films or magnetic clusters can be unambiguously excluded [39–41] (Supplementary Note S2). In addition, XMCD results are also presented next to safely exclude these extrinsic effects.

The element-specific XMCD was further performed to probe the localized magnetism. Left (blue) and right (red) circularly polarized X-rays, denoted as μ^+ and μ^- , were used to resolve the XMCD signals, which was in parallel to the external magnetic field and in the normal incidence with respect to the sample surface (Fig. 3a inset). The XMCD signals were obtained by taking the difference of the X-ray absorption spectroscopy (XAS) spectra, i.e. $\text{XMCD} = \mu^- - \mu^+$. The XAS spectra obtained in total-fluorescence yield mode were subtracted by a two-step function [42] and

a strong XMCD signal was acquired at 300 K, as shown in Fig. 3a. The agreement with the XAS of Fe_3GeTe_2 bulk crystals [43] in the spectra shape further confirms its intrinsic high T_C ferromagnetism in the doped films, possessing two similar sites of Fe with such crystals [44–47]. The lower the temperature, the stronger the observed XMCD intensity (Fig. 3b). Here, to estimate the magnetic order, the XMCD percentage β , defined as the intensity ratio of XMCD to XAS in the equation $\beta = \frac{(\mu^- - \mu^+)}{(\mu^- + \mu^+)}$, is utilized as a parameter, which is calculated to be $(10.9 \pm 1.0)\%$ and $(1.5 \pm 0.1)\%$ for the two peaks at L_3 edge. As the critical peak on the left side of Fe L_3 edge (marked as P1) gives the strongest dichroism, which suggests a larger magnetic contribution, we focus on P1 during the XMCD analyses. As shown in Fig. 3c, the temperature-dependent XMCD percentages can be fitted with an empirical function $(1 - T/T_C)^\gamma$ to extract the Curie temperature [48,49], based on which T_C is determined to be 313.3 ± 9.5 K. These results confirm our findings regarding the above-room-temperature ferromagnetism in $\text{Fe}_{3+1.80}\text{GeTe}_2$. In

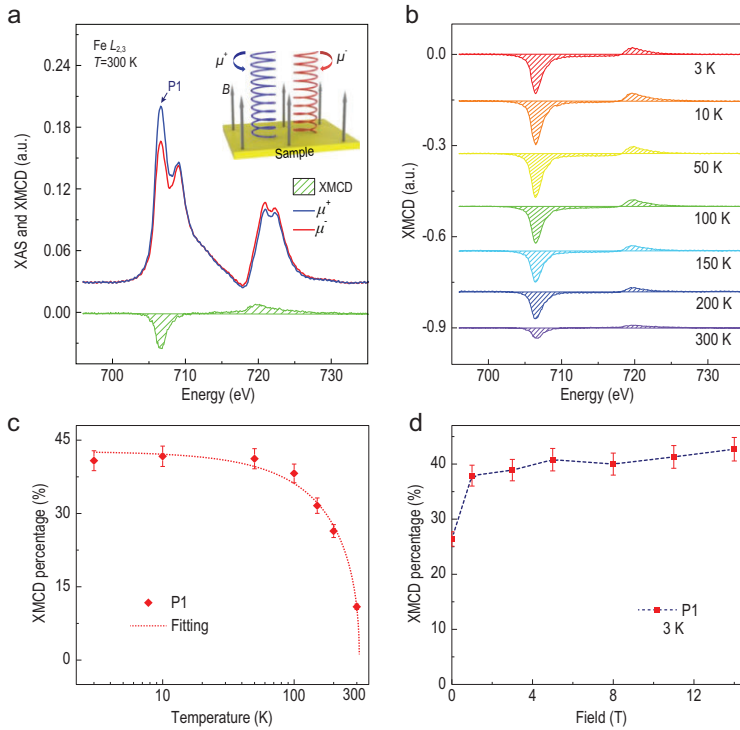


Figure 3. XAS spectra and XMCD signals of an $\text{Fe}_{3+1.80}\text{GeTe}_2$ sample at $\text{Fe } L_{2,3}$ edges. (a) Room-temperature XAS and XMCD spectra of $\text{Fe } L_{2,3}$ edges at the field of 5T. The agreement with the XAS of Fe_3GeTe_2 bulks [43] in the spectra shape further confirms the intrinsic room-temperature ferromagnetism. The two peaks at the $\text{Fe } L_3$ edge suggest two sites of Fe, with the XMCD percentages calculated to be $(10.90 \pm 1.0)\%$ and $(1.47 \pm 0.1)\%$, respectively. Inset, schematic of the XMCD experiments. (b) Temperature-dependent XMCD of $\text{Fe } L_{2,3}$ edges where the spectra at different temperatures have vertical offsets for clarity. The magnetic field is fixed at 5T. (c) XMCD percentage versus temperature. As the temperature rises, the XMCD percentage decreases continuously. The dashed lines represent the XMCD percentages fitting to the empirical equation $(1 - T/T_C)^\gamma$. T_C values are determined to be $313.3 \pm 9.5\text{ K}$, which further confirms the above-room-temperature ferromagnetism in $\text{Fe}_{3+1.80}\text{GeTe}_2$. (d) Field-dependent XMCD percentage, showing a large remanent XMCD percentage of 26.7% at zero-field.

addition, solid ferromagnetism can be identified with a strong remanent XMCD percentage of 26.4% under zero magnetic field at 3 K (Fig. 3d).

TUNABLE MAGNETISM AND THEORETICAL CALCULATION

In stark contrast to the continuously-decreased T_C in Fe-deficient $\text{Fe}_{3-\delta}\text{GeTe}_2$ samples [34,35] where the Fe composition deviates negatively ($\delta < 0.3$) from Fe_3GeTe_2 , here we present a large enhancement of the ferromagnetic order in $\text{Fe}_{3+X}\text{GeTe}_2$ films by systematically tuning the X value from -0.25 (Fe-deficient) to 2.80 (Fe-rich). As illustrated in Fig. 4a, T_C initially increases with the increasing Fe doping, reaches a maximum value of 320 K at $X = 1.80$ and finally drops to 290 K in

$\text{Fe}_{3+2.80}\text{GeTe}_2$. This T_C behavior is a prominent extension to that of the Fe-deficient $\text{Fe}_{3-\delta}\text{GeTe}_2$ samples. Utilizing the high- T_C and large-scale thin films, we have built MTJ device arrays (Fig. 4a inset) with an $\text{Fe}_{3+0.76}\text{GeTe}_2/\text{MgO}/\text{Fe}_3\text{GeTe}_2$ device structure (Supplementary Note S4). Clear tunneling magnetoresistance signals can be detected as the magnetic field scans back and forth. However, the tunneling magnetoresistance ratio is still low ($\sim 0.25\%$), which calls for further improvements on the crystalline quality of MgO.

In order to provide insight into the observed room-temperature ferromagnetic behavior in $\text{Fe}_{3+X}\text{GeTe}_2$ films, we performed DFT calculations within the LSDA + U framework to understand the bulk Fe_3GeTe_2 and its doping effect (Supplementary Note S5 and Fig. S17). We chose four different magnetic states, namely, the FM, AFM1, AFM2 and inter-AFM states, as illustrated in Fig. 4b. For the bulk, the LSDA + U calculations using the experimental lattice parameters confirm the FM ground state as summarized in Table 1. It is more stable than the inter-AFM state by 18 meV per formula unit (f.u.), indicating a relatively weak ferromagnetic interlayer coupling associated with the van der Waals bonding of the 2D material. However, due to the metallic behavior of Fe_3GeTe_2 , the intralayer itinerant FM is quite strong. Compared with the FM ground state, the AFM1 state lies much higher in energy (by 300 meV/f.u.). This energy cost is due to the suppressed electron itinerancy in the AFM1 state (with one AFM Fe1-Fe3-Fe1 zigzag channel, see Fig. 4b) and the corresponding reduced kinetic energy gain. If two AFM zigzag channels (Fe1-Fe3-Fe1 and Fe2-Fe3-Fe2, see Fig. 4b) appear as in the AFM2 state, the energy cost is calculated to be 624 meV/f.u., being nearly doubled compared with the AFM1-FM energy difference with the change of one magnetic channel. Therefore, in our calculations, we employed the AFM1-FM energy difference to characterize the stability of the FM ground state and to trace the varying FM stability with the changing Fe concentrations.

Owing to the van der Waals layered structure of Fe_3GeTe_2 , the additional Fe atoms most probably lie in the interlayer interstitial region. We use LSDA + U calculations to search the stable interlayer interstitial positions by optimizing the c -axis lattice parameter and atomic z coordinates. Our calculations find that, for a doped Fe atom, there are three most stable interlayer occupation positions on the 1×1 plane, (0,0), (1/3,2/3) and (2/3,1/3), which have almost the same potential well depth, as seen in Fig. 4c. This finding explains why the Fe concentration in $\text{Fe}_{3+X}\text{GeTe}_2$ can experimentally be largely enhanced.

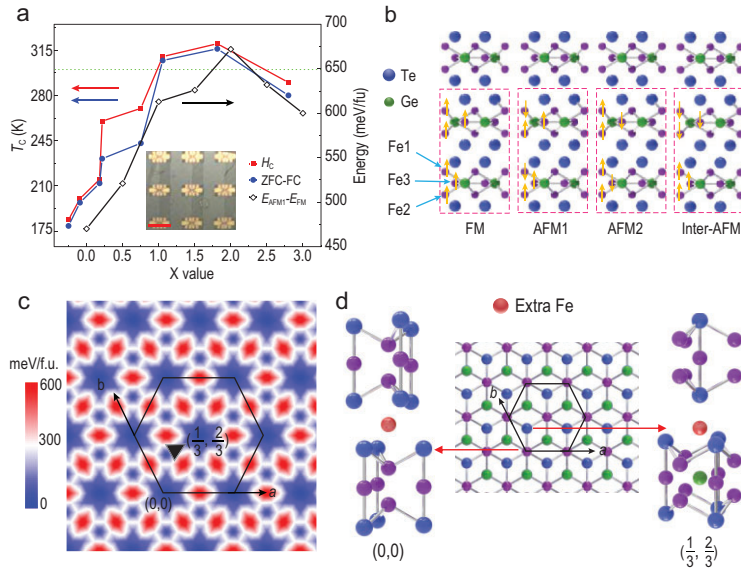


Figure 4. T_C modulation in $\text{Fe}_{3+X}\text{GeTe}_2$ film via Fe composition and DFT calculations. (a) T_C versus X ratio, reaching a peak value of 320 K at $X = 1.80$. Inset: an optical image of MTJ device arrays. The scale bar is $2 \mu\text{m}$. (b) Schematic diagrams for the four defined magnetic states, the orange arrows illustrating the spin direction of each Fe1, Fe2 and Fe3 atom. (c) Relative total energies map of an extra Fe atom in the different interlayer positions of Fe_3GeTe_2 calculated by LSDA + U. There are three most stable sites at (0,0), (1/3,2/3) and (2/3,1/3). (d) Local structure of an extra Fe at (0,0) or (1/3,2/3) in bulk Fe_3GeTe_2 .

Table 1. Relative total energy (meV/f.u.) and local spin moments (μ_B) of different magnetic states calculated by LSDA + U for bulk Fe_3GeTe_2 .

Magnetic state	ΔE (meV/f.u.)	Fe1 (μ_B)	Fe2 (μ_B)	Fe3 (μ_B)
FM	0	2.74	2.74	1.96
AFM1	300	-2.74	2.62	1.77
AFM2	624	2.88	2.88	-1.64
Inter-AFM	18	2.72	2.72	1.95

To study the impact of the doped interlayer Fe atoms on the magnetism of $\text{Fe}_{3+X}\text{GeTe}_2$, we first compare the two cases of $\text{Fe}_{3+0.5}\text{GeTe}_2$ with one doped Fe atom on either the (0,0) or (1/3,2/3) position (Fig. 4d), using the LSDA + U calculations including a full atomic relaxation. The AFM1-FM energy difference is calculated to be 530 and 521 meV/f.u., respectively, showing insignificant site dependence of the FM strength in $\text{Fe}_{3+0.5}\text{GeTe}_2$ on the interlayer Fe positions. We then simulate $\text{Fe}_{3+X}\text{GeTe}_2$ ($X = 0.5-3$) by adding the interlayer Fe atoms in the AB stacking Fe_3GeTe_2 unit cell one by one, at A(1/3,2/3), B(2/3,1/3), A(2/3,1/3), B(1/3,2/3), A(0,0) and B(0,0), to minimize the interlayer Fe-Fe coordinations in each case. As seen in Fig. 4a, upon increasing the interlayer Fe concentrations, the calculated AFM1-FM energy difference increases from 470 meV/f.u. (after atomic relaxation) for

the stoichiometric Fe_3GeTe_2 to the maximal 670 meV/f.u. for $X = 2$ and then drops to 600 meV/f.u. for $X = 3$. The maximal enhancement of the FM strength by $\sim 40\%$ at the optimal concentration $X = 2$ agrees well with our experimental findings. This composition-dependent T_C in $\text{Fe}_{3+X}\text{GeTe}_2$ films correlates with the electron doping effect which enhances the itinerant FM up to an optimal doping level (Supplementary Note S6).

CONCLUSION

In summary, we have demonstrated a direct doping approach in MBE growth to achieve high- T_C 2D ferromagnetic $\text{Fe}_{3+X}\text{GeTe}_2$ films beyond room temperature. Through systematically tuning the Fe composition, T_C experiences an efficient modulation from 185 K to 320 K, which arrives at the peak value of 320 K at $\text{Fe}_{3+1.80}\text{GeTe}_2$, validated by the temperature-dependent XMCD measurements. We further demonstrated large-scale MTJ device arrays based on $\text{Fe}_{3+X}\text{GeTe}_2$ films. Moreover, our DFT study suggests that the doped interlayer Fe atoms provide a strong tunability to the magnetic order, achieving the optimal enhancement of FM strength by 40% at $X = 2$. Therefore, this study opens an avenue to a significant enhancement of the T_C in emerging 2D ferromagnetic $\text{Fe}_{3+X}\text{GeTe}_2$ films, which may facilitate their practical application in spintronic devices.

METHODS

Thin film synthesis and characterization

$\text{Fe}_{3+X}\text{GeTe}_2$ thin films were synthesized on (0001)-sapphire in a Perkin Elmer 430 MBE system (base vacuum: $\sim 2.5 \times 10^{-9}$ Torr). The substrates were firstly cleaned using a standard process, and before the growth, substrates were annealed at 600°C for 30 minutes, which was then cooled to the target temperature of 340°C . The growth temperatures for Ge-cell and Te-cell were 1020°C and 285°C , and the Fe composition was tuned via varying the Fe-cell temperature. The crystal oscillator was used to measure each element's flux. XRD results were measured in a Bruker D8 Discover facility and transmission electron microscope measurements were performed using JEOL JEM-ARM 200F and FEI Titan G2 systems.

Electrical and magnetization measurement

Magnetotransport results were collected by SR830 in the Physical Properties Measurement System (PPMS) and the devices were in the six-Hall-bar

geometry. The magnetization measurements were accomplished by DC-Superconducting-Quantum-Interface-Devices (SQUID) by Quantum Design.

RMCD and XMCD measurements

RMCD measurements were performed in a closed-cycle helium cryostat with measurable temperature ranges from 15 to 287 K. A 633 nm HeNe laser with the power of $\sim 0.3 \mu\text{W}$ and the focused beam spot of $3 \mu\text{m}$ was in the normal incidence onto the sample. A lock-in amplifier was utilized to acquire the RMCD signals. XMCD measurements at Fe $L_{2,3}$ edge were performed on beamline I10 at the Diamond Light Source.

DFT calculation

DFT calculations were processed using the Vienna *ab initio* Simulation Package (VASP) [50,51]. Local density approximation to the exchange-correlation function was used [52], which has previously been shown to describe the structural properties of Fe_3GeTe_2 well [53]. A plane wave cut-off of at least 400 eV was employed. The Brillouin zone was sampled using an $8 \times 8 \times 3$ k-point mesh. The ionic potentials, including the effect of core electrons, were described by the projector augmented wave method [54]. The atomic relaxations were implemented until the Hellmann-Feynman force on each atom was smaller than $0.01 \text{ eV}/\text{\AA}$. We used the experimental lattice constants with atomic relaxations to study the magnetism of $\text{Fe}_{3+x}\text{GeTe}_2$. In addition to LSDA, the LSDA plus Hubbard U (LSDA + U) method was employed [51], and we chose $U = 3.5 \text{ eV}$ (and Hund exchange $J = 0.9 \text{ eV}$) for the Fe 3d electrons to calculate the magnetic properties. The calculation details are shown in Supplementary Note S6.

SUPPLEMENTARY DATA

Supplementary data are available at [NSR](#) online.

ACKNOWLEDGEMENTS

We acknowledge the Diamond Light Source for the XMCD measurements (Proposal SI20748). Part of the sample fabrication was performed at Fudan Nano-Fabrication Laboratory.

FUNDING

This work was supported by the National Key Research and Development Program of China (2017YFA0303302, 2018YFA0305601, 2016YFA0300700 and 2017YFA0206304), the National Natural Science Foundation of China (11934005, 61322407, 11874116, 11474059, 11674064, 61427812 and 11774160), the Science and Technology Commission of Shanghai (19511120500), the Shanghai Municipal Science

and Technology Major Project (2019SHZDZX01), the Program of Shanghai Academic/Technology Research Leader (20XD1400200), the Beijing Natural Science Foundation (Z180014), the National Basic Research Program of China (2014CB921101 and 2016YFA0300803), the UK EPSRC (EP/S010246/1), the Australian Research Council, the Progress 100 program to encourage the UQ-KU collaboration and the Japanese Nanotechnology Platform Project for advanced nanostructure characterization (JPMXP09-A-19-KU-0312). E.Z. acknowledges support from the China Postdoctoral Innovative Talents Support Program (BX20190085) and the China Postdoctoral Science Foundation (2019M661331). S.L. acknowledges support from the China Postdoctoral Science Foundation (2020TQ0080 and 2020M681138). A.N. acknowledges support from the startup grant (SG/MHRD-19-0001) of the Indian Institute of Science. The work at the University of Washington is supported by the Department of Energy, Basic Energy Sciences, Materials Sciences and Engineering Division (DE-SC0018171).

AUTHOR CONTRIBUTIONS

F.X. and H.W. conceived the ideas and F.X. supervised the overall research. S.L., Z.L., X.G. and W.B. synthesized high-quality $\text{Fe}_{3+x}\text{GeTe}_2$ thin films and fabricated the devices. S.L., Z.L., E.Z., Y.Y., L.A. and C.H. performed the PPMS measurements. S.L., E.Z., Q.L., L.Y. and J.S. processed the transport and SQUID data. J.Z. and X.X. carried out the RMCD measurement and analysis. X.Z., W.L., J.S. and Y.X. performed the XMCD measurement and analyzed the XMCD data. K.Y. and H.W. carried out DFT calculations and theoretical analyses of different magnetic states. Z.L., M.K., T.T., Q.D., Y.C., X.H., S.M. and J.Z. did the transmission electron microscopy characterizations and analysis. S.L., Z.L., K.Y., A.N., H.W. and F.X. wrote the paper with assistance from all other authors.

Conflict of interest statement. None declared.

REFERENCES

- Novoselov KS, Geim AK and Morozov SV *et al.* Two-dimensional gas of massless Dirac fermions in graphene. *Nature* 2005; **438**: 197–200.
- Wang QH, Kalantar-Zadeh K and Kis A *et al.* Electronics and optoelectronics of two-dimensional transition metal dichalcogenides. *Nat Nanotechnol* 2012; **7**: 699–712.
- Saito Y, Nojima T and Iwasa Y. Highly crystalline 2D superconductors. *Nat Rev Mater* 2016; **2**: 16094.
- Huang B, Clark G and Navarro-Moratalla E *et al.* Layer-dependent ferromagnetism in a van der Waals crystal down to the monolayer limit. *Nature* 2017; **546**: 270–3.
- Chang K, Liu J and Lin H *et al.* Discovery of robust in-plane ferroelectricity in atomic-thick SnTe. *Science* 2016; **353**: 274–8.
- Tong Q, Liu F and Xiao J *et al.* Skyrmions in the Moiré of van der Waals 2D magnets. *Nano Lett* 2018; **18**: 7194–9.
- Kim K, Seo J and Lee E *et al.* Large anomalous Hall current induced by topological nodal lines in a ferromagnetic van der Waals semimetal. *Nat Mater* 2018; **17**: 794–9.
- Zhang J, Zhao B and Yao Y *et al.* Robust quantum anomalous Hall effect in graphene-based van der Waals heterostructures. *Phys Rev B* 2015; **92**: 165418.

9. Sivasdas N, Okamoto S and Xu X *et al.* Stacking-dependent magnetism in bilayer CrI₃. *Nano Lett* 2018; **18**: 7658–64.
10. Jiang P, Wang C and Chen D *et al.* Stacking tunable interlayer magnetism in bilayer CrI₃. *Phys Rev B* 2019; **99**: 144401.
11. Jiang P, Li L and Liao Z *et al.* Spin direction-controlled electronic band structure in two-dimensional ferromagnetic CrI₃. *Nano Lett* 2018; **18**: 3844–9.
12. Jiang S, Li L and Wang Z *et al.* Controlling magnetism in 2D CrI₃ by electrostatic doping. *Nat Nanotechnol* 2018; **13**: 549–53.
13. Wang H, Fan F and Zhu S *et al.* Doping enhanced ferromagnetism and induced half-metallicity in CrI₃ monolayer. *Europhys Lett* 2016; **114**: 47001.
14. Ghazaryan D, Greenaway MT and Wang Z *et al.* Magnon-assisted tunneling in van der Waals heterostructures based on CrBr₃. *Nat Electron* 2018; **1**: 344–9.
15. Song T, Cai X and Tu MW-Y *et al.* Giant tunneling magnetoresistance in spin-filter van der Waals heterostructures. *Science* 2018; **340**: 1214–8.
16. Klein DR, MacNeill D and Lado JL *et al.* Probing magnetism in 2D van der Waals crystalline insulators via electron tunneling. *Science* 2018; **360**: 1218–22.
17. Wang Z, Gutiérrez-Lezama I and Ubrig N *et al.* Very large tunneling magnetoresistance in layered magnetic semiconductor CrI₃. *Nat Commun* 2018; **9**: 2516.
18. Leon-Brito N, Bauer ED and Ronning F *et al.* Magnetic microstructure and magnetic properties of uniaxial itinerant ferromagnet Fe₃GeTe₂. *J Appl Phys* 2016; **120**: 083903.
19. Deng Y, Yu Y and Song Y *et al.* Gate-tunable room-temperature ferromagnetism in two-dimensional Fe₃GeTe₂. *Nature* 2018; **563**: 94–9.
20. Chang G, Singh B and Xu S-Y *et al.* Magnetic and noncentrosymmetric Weyl fermion semimetals in the RAlGe family of compounds (R = rare earth). *Phys Rev B* 2018; **97**: 041104.
21. Ueda K, Fujioka J and Takahashi Y *et al.* Anomalous domain-wall conductance in pyrochlore-type Nd₂IrO₇ on the verge of the metal-insulator transition. *Phys Rev B* 2014; **89**: 075127.
22. Xu G, Weng H and Wang Z *et al.* Chern semimetal and the quantized anomalous Hall effect in HgCr₂Se₄. *Phys Rev Lett* 2011; **107**: 186806.
23. Chang G, Xu S-Y and Zheng H *et al.* Room-temperature magnetic topological Weyl fermion and nodal line semimetal states in half-metallic Heusler Co₂TiX (X = Si, Ge, or Sn). *Sci Rep* 2016; **6**: 38839.
24. Erwin SC, Zu L and Haftel MI *et al.* Doping semiconductor nanocrystals. *Nature* 2005; **436**: 91–4.
25. Liu H, Liu Y and Zhu D. Chemical doping of graphene. *J Mater Chem* 2011; **21**: 3335–45.
26. Mann J, Ma Q and Odenthal PM *et al.* 2-Dimensional transition metal dichalcogenides with tunable direct band gaps: MoS_{2(1-x)}Se_{2x} monolayers. *Adv Mater* 2014; **26**: 1399–404.
27. Chen Y, Xi J and Dumcenco DO *et al.* Tunable band gap photoluminescence from atomically thin transition-metal dichalcogenide alloys. *ACS Nano* 2013; **7**: 4610–6.
28. Klee V, Preciado E and Barroso D *et al.* Superlinear composition-dependent photocurrent in CVD-grown monolayer MoS_{2(1-x)}Se_{2x} alloy devices. *Nano Lett* 2015; **15**: 2612–9.
29. Liu S, Yuan X and Wang P *et al.* Controllable growth of vertical heterostructure GaTe_xSe_{1-x}/Si by molecular beam epitaxy. *ACS Nano* 2015; **9**: 8592–8.
30. Chang C-Z, Zhang J and Feng X *et al.* Experimental observation of the quantum anomalous Hall effect in a magnetic topological insulator. *Science* 2013; **340**: 167–70.
31. Ku KC, Potashnik SJ and Wang RF *et al.* Highly enhanced Curie temperature in low-temperature annealed [Ga,Mn]As epilayers. *Appl Phys Lett* 2003; **82**: 2302–4.
32. Dietl T and Ohno H. Dilute ferromagnetic semiconductors: physics and spintronic structures. *Rev Mod Phys* 2014; **86**: 187–251.
33. Zhu X, Guo Y and Cheng H *et al.* Signature of coexistence of superconductivity and ferromagnetism in two-dimensional NbSe₂ triggered by surface molecular adsorption. *Nat Commun* 2016; **7**: 11210.
34. May AF, Calder S and Cantoni C *et al.* Magnetic structure and phase stability of the van der Waals bonded ferromagnet Fe_{3-x}GeTe₂. *Phys Rev B* 2016; **93**: 014411.
35. Liu S, Yuan X and Zou Y *et al.* Wafer-scale two-dimensional ferromagnetic Fe₃GeTe₂ thin films grown by molecular beam epitaxy. *npj 2D Mater Appl* 2017; **1**: 30.
36. Deiseroth H-J, Aleksandrov K and Reiner C *et al.* Fe₃GeTe₂ and Ni₃GeTe₂—two new layered transition-metal compounds: crystal structures, HRTEM investigations, and magnetic and electrical properties. *Eur J Inorg Chem* 2006; **2006**: 1561–7.
37. Liu S, Yang K and Liu W *et al.* Two-dimensional ferromagnetic superlattices. *Natl Sci Rev* 2020; **7**: 745–54.
38. Tan C, Lee J and Jung S-G *et al.* Hard magnetic properties in nanoflake van der Waals Fe₃GeTe₂. *Nat Commun* 2018; **9**: 1554.
39. Qiu ZQ, Pearson J and Bader SD. Asymmetry of the spin reorientation transition in ultrathin Fe films and wedges grown on Ag(100). *Phys Rev Lett* 1993; **70**: 1006–9.
40. Gradmann U. Magnetic surface anisotropies. *J Magn Magn Mater* 1986; **54–7**: 733–6.
41. Billas IML, Châtelain A and de Heer WA. Magnetism of Fe, Co and Ni clusters in molecular beams. *J Magn Magn Mater* 1997; **168**: 64–84.
42. Chen CT, Idzerda YU and Lin H-J *et al.* Experimental confirmation of the X-ray magnetic circular dichroism sum rules for iron and cobalt. *Phys Rev Lett* 1995; **75**: 152–5.
43. Zhu J-X, Janoschek M and Chaves DS *et al.* Electronic correlation and magnetism in the ferromagnetic metal Fe₃GeTe₂. *Phys Rev B* 2016; **93**: 144404.
44. Claydon JS, Xu YB and Tselepi M *et al.* Direct observation of a bulklike spin moment at the Fe/GaAs(100) — 4 × 6 interface. *Phys Rev Lett* 2004; **93**: 037206.
45. Kuneš J and Oppeneer PM. Anisotropic X-ray magnetic linear dichroism at the L_{2,3} edges of cubic Fe, Co, and Ni: ab initio calculations and model theory. *Phys Rev B* 2003; **67**: 024431.
46. Weser M, Voloshina EN and Horn K *et al.* Electronic structure and magnetic properties of the graphene/Fe/Ni(111) intercalation-like system. *Phys Chem Chem Phys* 2011; **13**: 7534–9.
47. Nolle D, Goering E and Tietze T *et al.* Structural and magnetic deconvolution of FePt/FeOx nanoparticles using X-ray magnetic circular dichroism. *New J Phys* 2009; **11**: 033034.
48. Ormaza M, Fernández L and Ilyn M *et al.* High temperature ferromagnetism in a GdAg₂ monolayer. *Nano Lett* 2016; **16**: 4230–5.
49. Ye M, Li W and Zhu S *et al.* Carrier-mediated ferromagnetism in the magnetic topological insulator Cr-doped (Sb,Bi)₂Te₃. *Nat Commun* 2015; **6**: 8913.
50. Kresse G and Furthmüller J. Efficient iterative schemes for ab initio total-energy calculations using a plane-wave basis set. *Phys Rev B* 1996; **54**: 11169–86.
51. Anisimov VI, Aryasetiawan F and Lichtenstein AI. First-principles calculations of the electronic structure and spectra of strongly correlated systems: the LDA + U method. *J Phys Condens Matter* 1997; **9**: 767.
52. Perdew JP and Zunger A. Self-interaction correction to density-functional approximations for many-electron systems. *Phys Rev B* 1981; **23**: 5048–79.
53. Zhuang HL, Kent PRC and Hennig RG. Strong anisotropy and magnetostriction in the two-dimensional Stoner ferromagnet Fe₃GeTe₂. *Phys Rev B* 2016; **93**: 134407.
54. Kresse G and Joubert D. From ultrasoft pseudopotentials to the projector augmented-wave method. *Phys Rev B* 1999; **59**: 1758–75.